APPLIED SCIENCES AND ENGINEERING

μSonic-hand: Biomedical micromanipulation driven by acoustic gas-liquid-solid interactions

Xiaoming Liu[1]*†, Yuyang Li[1,2]*†, Fengyu Liu[1], Qing Shi[1], Lixin Dong[3], Qiang Huang[1]*, Tatsuo Arai[1,4], Toshio Fukuda[5]

Micromanipulation is crucial for operating and analyzing microobjects in advanced biomedical applications. However, safe, low-cost, multifunctional micromanipulation for operating bio-objects across scales and modalities remains inaccessible. Here, we propose a versatile micromanipulation method driven by acoustic gas-liquid-solid interactions, named μSonic-hand. The bubble contained at the end of a micropipette and the surrounding liquid form a gas-liquid multiphase system susceptible to acoustic waves. Driven by a piezoelectric transducer, the oscillating gas-liquid interface induces acoustic microstreaming, markedly increasing the mass transfer efficiency. It enables multiple liquid micromanipulations, including mixing, dispersion, enhancing cell membrane permeability, and harvesting selected cells. Furthermore, a controllable three-dimensional axisymmetric vortex in an open environment overcomes the constraints of microfluidic chip, enabling stable trapping, rapid transportation, and multidirectional rotation of HeLa cells, embryos, and other bio-objects ranging from micrometers to millimeters. A variety of applications demonstrate that the μSonic-hand, with its wide-range capabilities, inherent biocompatibility, and extremely low cost could remarkably advance biomedical science.

INTRODUCTION

As our knowledge of the microscopic realm deepens, advanced tools become increasingly vital for understanding and interacting with microobjects. Among these tools, micromanipulation is one of the most critical techniques for operating and analyzing microobjects in advanced biological research and medical treatments, such as cloning, genetic research, single-cell analysis, cell therapy, and assisted reproduction (*1*–*5*). Nowadays, micromanipulations in biomedical laboratories commonly use motorized precision stages equipped with micropipettes or other customized end effectors, but the disappointingly poor success rates, the low ability in complex multiple tasks, and the extensive training required of operators do pose challenges to the development of the related biomedical science. Over the past two decades, researchers have been eagerly pursuing previously unexplored micromanipulation approaches, including investigating more reliable ways of achieving controllable microscale interactions and developing advanced robotic operation strategies (*6*–*12*). However, a safe, low-cost, multifunctional micromanipulation method for operating biomedical objects across scales and modalities is not yet accessible.

Micromanipulation is the physical interaction with microobjects under a microscope, mainly performed by high-precision movement mechanism and micro end effector (*13*). Most research on micromanipulation focuses on developing various end effectors for simple grasping and translational operations, while few rotation methods have been proposed, although rotational motions are more ubiquitous throughout nature, particularly at the microscale (*14*). Apart from immobilization, transportation, rotation, and combinations of these basic operations of the individual entities, manipulating liquid at the microscale is also indispensable in most biomedical and chemical laboratory processes. However, liquid micromanipulation, such as the micromixing, the nano-/picoliter liquid injection, and the controlled pumping of local flow, is often omitted from the developmental functions of an emergent micromanipulation method because liquid micromanipulation is even more challenging due to the low Reynolds numbers. The development of a micromanipulation method capable of manipulating both liquids and individual biological entities holds significant potential for advancing medical research.

Micromanipulation based on direct mechanical contact is popular, but difficult release processes attributed to notable adhesion at the microscale and potential damages to living microorganisms caused by frequent mechanical contact lead to low efficiency and low success rates in biomedical micromanipulation (*15*–*17*). Over the past decades, electric, magnetic, and optical field forces have been used to circumvent the difficult release processes and renew the physical interactions in micromanipulation (table S1) (*18*–*22*). However, these field-driven interactions heavily depend on the specific physical structure and properties of the manipulated objects, making them unsuitable for diverse cross-scale biological samples. Potential damage resulting from the direct illumination with intense lasers, the heating effects of electric fields, and cell magnetization obtained by the intrusion of external magnetic materials further limit their applications in manipulating living biological samples. Furthermore, systems for generating these external fields are huge and complex, particularly for tasks demanding large workspaces, challenging the deployment on general-purpose microscopes and the operation by biomedical participants. Hydrodynamic micromanipulation has shown outstanding biocompatibility in numerous biomedical applications involving microfluidic chips, wherein fluidic fields are induced and regulated through specifically designed geometric features (*23*–*27*). However, the closed environment of the

[1]Key Laboratory of Biomimetic Robots and Systems, Ministry of Education, State Key Laboratory of Intelligent Control and Decision of Complex System, and School of Mechatronical Engineering, Beijing Institute of Technology, Beijing 100081, China. [2]Key Laboratory of Intelligent Flexible Actuation and Control in Universities of Jiangsu Province and School of Mechanical Engineering, Jiangsu University, Zhenjiang 212013, China. [3]Department of Biomedical Engineering, City University of Hong Kong, Hong Kong 999077, China. [4]Center for Neuroscience and Biomedical Engineering, The University of Electro-Communications, Tokyo, 1828585, Japan. [5]Institute of Innovation for Future Society, Nagoya University, Nagoya, 4648601, Japan.
*Corresponding author. Email: liuxiaoming555@bit.edu.cn (X.L.); leeyunth@bit.edu.cn (Y.L.); qhuang@bit.edu.cn (Q.H.)
†These authors contributed equally to this work.

microfluidic chip poses challenges to the integration of other functional units and limits the degrees of freedom in operations. Inner fixed geometries of the microfluidic chip tailored to the size of the manipulated objects restrict the capability of performing various operations of multiscale objects under the microscope. A more biocompatible micromanipulation method is therefore demanded to operate the cross-scale objects with more degrees of freedom in an open environment.

Acoustohydrodynamic micromanipulation emerges as a promising method for manipulating liquids and individual entities at the microscale, offering versatility, simplicity, high biocompatibility, and low energy requirements (*28*–*32*). The acoustic waves with adjustable frequency and amplitude, serving as the energy source, enable multifunctional manipulation of objects ranging from micrometers to millimeters. However, the acoustohydrodynamic micromanipulation is often performed in a microfluidic chip, using the confinement of the microchannel to optimize its low controllability. Furthermore, most acoustohydrodynamic manipulations are driven by two-dimensional (2D) acoustic streaming, which is inadequate for cross-plane transportation and multidirectional rotation. Recent studies by our team and other researchers have shown that vibrating end effectors mounted on motorized precision stages can induce microflow in an open environment, facilitating micromanipulation while ensuring good biocompatibility, offering multiple functions, and enabling efficient robotic operations (*33*, *34*). Inducing and controlling 3D acoustic microstreaming in an open environment could be pivotal in developing a versatile micromanipulation tool with high degrees of freedom for biomedical applications.

This paper presents a versatile acoustohydrodynamic microhand (μSonic-hand) based on gas-liquid-solid interactions. A bubble housed at the tip of a micropipette, along with the surrounding liquid, constitutes a gas-liquid multiphase system highly responsive to acoustic waves. Stimulated by a piezoelectric transducer, the oscillating gas-liquid interface generates controllable acoustic microstreaming with a defined pattern, greatly enhancing mass transfer efficiency at the microscale. It enables multiple liquid micromanipulations, including mixing, dispersion, enhancing cell membrane permeability, and harvesting target cells. Furthermore, controllable 3D axisymmetric vortex and secondary acoustic radiation forces overcome constraints on the operations in microfluidic chips, enabling trapping, transportation, and rotation of biological organisms ranging from micrometers to millimeters. The μSonic-hand with these wide-range capabilities could have great potential in a variety of biomedical applications.

RESULTS

Acoustically driven gas-liquid-solid interactions

Acoustic waves exert periodic forces on objects that obstruct their propagation (*3*). Although the force generated by low doses of acoustic energy is generally imperceptible, multiphase systems are more susceptible to acoustic waves, particularly at the gas-liquid interface (*35*–*38*). The distinct response behavior of these multiphase bodies facilitates the selective release of acoustic energy, leading to robust gas-liquid interface oscillations. This phenomenon, in turn, triggers two fundamental factors of the acoustohydrodynamic manipulation process: acoustic streaming and acoustic radiation force.

The proposed μSonic-hand micromanipulation system comprises an acoustic source, a micropipette containing a bubble at the end, and a motorized precision stage, as shown in Fig. 1 and fig. S1. We use a piezoelectric transducer driven and tuned by a function generator to emit the desired acoustic waves. The glass slide, tightly bonded with the piezoelectric transducer, facilitates the transmission of acoustic waves to the droplet sample loaded onto it. The micropipette is connected to a pneumatic injector. Driven by negative

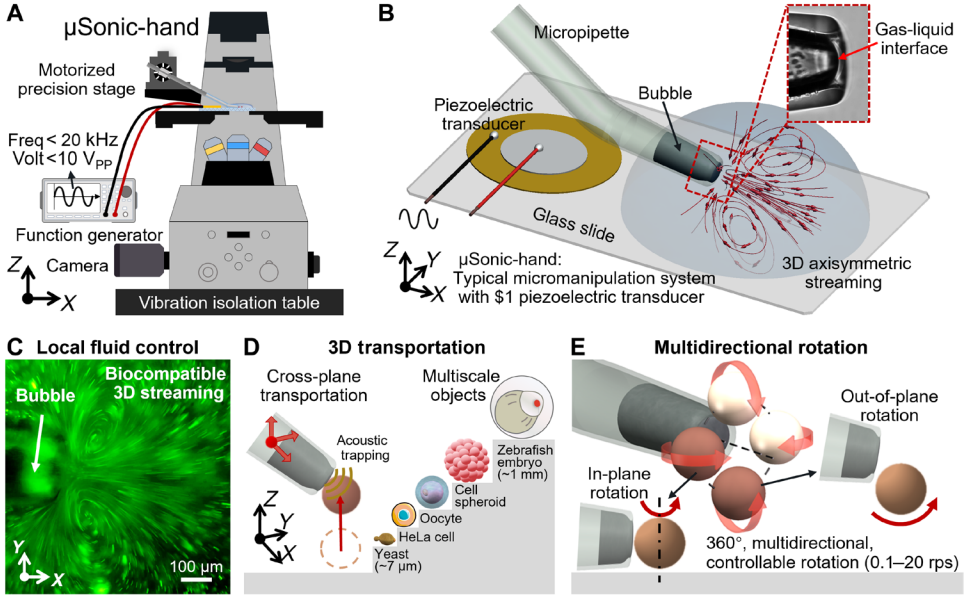

Fig. 1. Overview of the μSonic-hand. (**A**) μSonic-hand includes an additional piezoelectric transducer in a typical cell injection unit under the optical inverted microscope. (**B**) The gas-liquid interface oscillates in response to the acoustic waves emitted by the piezoelectric transducer, generating 3D axisymmetric streaming. (**C**) The generated local acoustic streaming with a 3D axisymmetric vortex pattern is visualized by the 1-μm polystyrene (PS) fluorescent particles (movie S1). (**D**) The acoustic radiation force enables the trapping and 3D transportation of cross-scale objects at the microscale. (**E**) Multidirectional rotation by altering the object's relative position in the axisymmetric vortex. rps, revolutions per second.

pressure, the micropipette first draws up a small amount of liquid and then moves out of the droplet to intake a specific amount of air. Upon returning the micropipette to the liquid, a micropipette with a microbubble contained at its end is obtained. Here, we fabricate the micropipette with a concave orifice, which is often used for holding cells by negative pressure in cell injection. The concave orifice can effectively enhance the stability of the curvature and position of the air-liquid interface by increasing the surface tension and adhesive force (fig. S2). The motorized precision stage facilitates robotic high-precision movement of the end effector. The configuration of the proposed μSonic-hand is a typical micromanipulation system with an additional piezoelectric transducer, enabling the proposed method to be easily deployed in a biological laboratory or an assisted reproduction laboratory owning a microscope equipped with the cell injection unit (fig. S3).

Here, the acoustic wave generated by the piezoelectric transducer is frequency modulated to match the bubble geometries, achieving resonance. To determine the resultant frequency, we applied a frequency sweep around the calculated theoretical resonant frequency (text S1) and took the applied frequency as the operation frequency when the maximum oscillation amplitude of the gas-liquid interface was observed. The resultant reciprocal oscillations at the air-liquid interface led to high-speed liquid recirculation, which eventually manifests itself in a microvortex, as evidenced by the second-order term of the Navier-Stokes equation (*39*, *40*). This phenomenon, known as acoustic streaming, is illustrated in Fig. 1 (B and C) and movie S1, displaying a 3D axisymmetric vortex pattern reminiscent of that generated by a swimming rotifer (*41*). The microstreaming velocity (u) can be regulated by adjusting the amplitude of the sinusoidal voltage (V) applied to the piezoelectric transducer (text S2). While the microstreaming may be amplified, reduced, or slightly distorted, it maintains the 3D axisymmetric vortex pattern. The offered high controllability and the simple underlying principles provide a solid foundation for carrying out a variety of manipulations driven by the induced acoustic axisymmetric vortex.

Simultaneously, the oscillating microbubble serves as an acoustic source due to the scattering effect of the incident wave, enabling it to attract and trap nearby objects via acoustic radiation forces (text S3). The bubble in the micropipette, the liquid surrounding the micropipette end, and the trapped object excite and influence each other, forming the gas-liquid-solid three-phase interactions. Order-of-magnitude calculations suggest that, for objects marginally denser than water (including most plant and animal cells), their buoyancy combined with the trapping force exerted by acoustic radiation is adequate to counteract gravity and fluid resistance (Fig. 1D). In addition, the vortex supplies adequate torque to rotate the spherical object, with the rotation axis adjustable by altering the object's relative position in the axisymmetric vortex (Fig. 1E). In this low Reynolds number environment (text S4), the acoustic streaming provides a torque balanced with the viscous torque, and the angular velocity Ω of the object matches the surrounding fluids. Furthermore, given the deterministic relationship between microstreaming velocity u and the input voltage V applied to the piezoelectric transducer, as $u \sim V^2$ (text S2), implying that the rotational velocity of the object is controllable.

Liquid manipulation via acoustic streaming

Microfluidic devices, known as micro total analysis system (μTAS) or lab-on-a-chip (LoC), are capable of obtaining sufficient sample information in limited quantities. Now, most μTASs are closed systems independent of traditional chemical and biological laboratory processes. The mass transfer between different fluids is enhanced by passive convective recirculation of fluids triggered by active perturbation or structural design (*25*, *42*, *43*). These methods often rely on the confinement of closed microfluidic channels, limiting access to other tools or processes and requiring lengthy preparation times. In addition, for droplets in an unconfined state, small sample volumes with low Reynolds numbers can markedly reduce mass transfer efficiencies, leading to inadequate mixing, dispersion, dissolution, and manipulation. The LoC is not the only way to manipulate and control the liquid at the microscale. The proposed μSonic-hand offers a viable solution to manipulate liquid in an open environment and address these limitations. The induced controllable acoustic microstreaming offers defined vortex patterns and adjustable flow velocities to manipulate various liquids and liquids containing particles or biological cells. The strong acoustic streaming can generate high fluid shear, substantially enhancing mass transfer efficiency and expediting liquid mixing, dispersion, and dissolution at the microscale.

Experiments using a mixture of deionized water and green fluorescently labeled polystyrene (PS) microspheres with a diameter of 1 μm, as shown in Fig. 1C and movie S2, clearly illustrated the axisymmetric vortex pattern. When the particle diameter is much smaller than that of the bubble, the streaming force predominates over the acoustic radiation force, accurately reflecting the streaming pattern. We confirmed the streaming pattern using numerical simulations, and the results aligned with experimental observations (Fig. 2A and text S3). The uniformly distributed particles circulate along the streaming with a high velocity, demonstrating the capability of high-speed microstreaming to disrupt fluid interfaces, enhance mass transport, and facilitate efficient microscale mixing (*44*, *45*). To evaluate the μSonic-hand's ability to mix high-viscosity liquids, we constructed an array of short polydimethylsiloxane (PDMS) micropillars on a hydrophobic glass surface for individual microreactions and precise microliter sample processing (fig. S4). We used egg white, a high-viscosity sample (approximately 200 mPa·s), as a test material. We dropped 10 μl of egg white containing 30% staining pigment into an equal volume of pure water to form a single droplet on the micropillar. We used the μSonic-hand to induce microstreaming and drive the motorized precision stage to move it along a programmed path to enhance mass transport throughout the entire droplet (Fig. 2A and fig. S5A). To illustrate the mixing effect of the μSonic-hand, we also performed spontaneous mixing and mixing by moving the micropipette without acoustic excitation. Quantitative analysis of the mixing efficiency (Materials and Methods) reveals that the μSonic-hand with acoustic excitation markedly enhances mixing (Fig. 2A).

Enhancing mass transfer can also expedite the dispersion of aggregated nanoparticles in the liquid. Nanoparticles aggregate in water due to their large inherent surface energy, notable van der Waals forces, and electrostatic forces. To demonstrate the efficacy of μSonic-hand in dispersing nanoparticles, untreated Fe_3O_4 particles with a diameter of 500 nm were proportionally added to an aqueous solution with a volume fraction of 15%. The dispersion followed the same strategy and path as the mixing experiments. Figure 2B illustrates the trapping and scattering of the aggregated particles by the μSonic-hand (fig. S5B and movie S2). In addition, we quantitatively characterize the dispersion by conducting statistical analyses of nanoparticle diameter and density per unit area. We observe the complete disappearance of large particles, a notable reduction in particle aggregation, and maintenance of this dispersion effect over time (Fig. 2B).

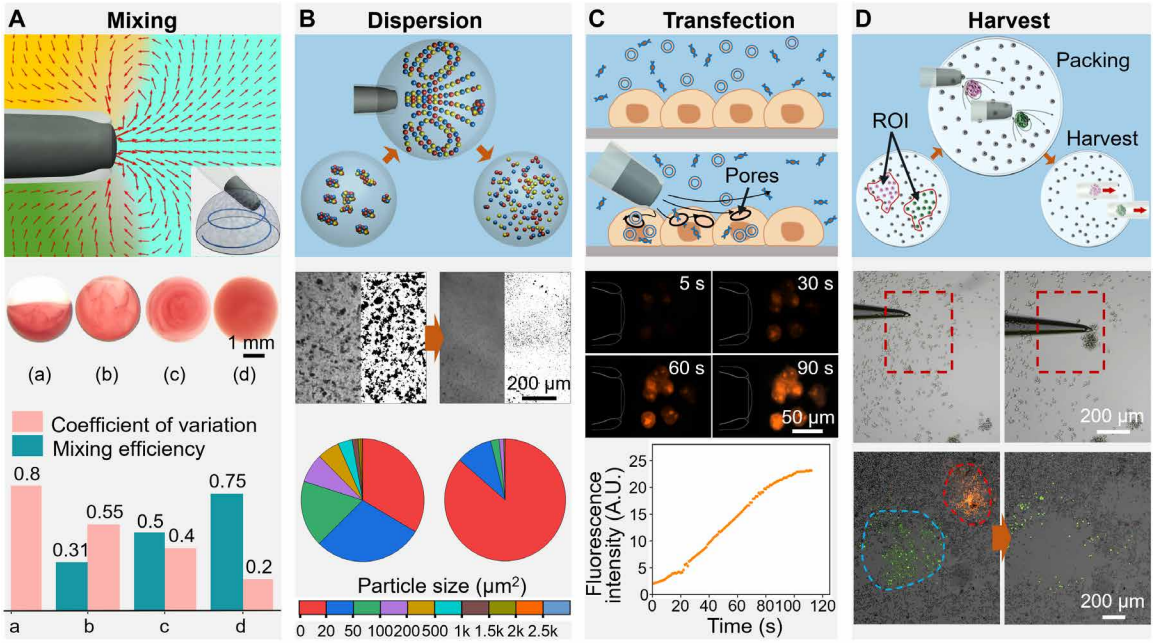

Fig. 2. Multiple liquid micromanipulations. (**A**) Mix high-viscosity liquids (egg white and pure water) by the local microstreaming (movie S2). The top figure shows the streaming pattern obtained by numerical simulations. In the middle figure, (a) represents the state before mixing, while (b), (c), and (d) represent spontaneous mixing, mixing by moving the micropipette without acoustic excitation, and mixing by moving the micropipette with acoustic excitation, respectively. All action times are 2 min. The bottom figure shows the quantitative analysis of the mixing efficiency (Materials and Methods). (**B**) Dispersion of aggregated nanoparticles in droplets (movie S2). The middle and bottom figures show the effect before and after treatment of untreated (agglomerated) Fe_3O_4 particles with a diameter of 500 nm and the quantitative analysis of the agglomeration sizes before and after treatment, respectively. (**C**) Fluid shear force enhances cell membrane permeability for transfection. The top figure shows that fluid shear stimulation creates transient pores in cell membranes, facilitating drug delivery and gene therapy. The middle and bottom figures show the accelerated entrance of propidium iodide (PI) stain into HeLa cells under the fluid shear stimulation and increasing fluorescence intensity over time (movie S2). A.U., arbitrary units. (**D**) Harvest target cells in the region of interest (ROI) by the μSonic-hand (movie S2). The middle figure shows that the cells were confined in the local vortex and packed into a cluster. The bottom figure shows the harvest of labeled green and orange cells (green cells stained with calcein-AM; orange cells stained with acridine orange).

The increase in fluid velocity also leads to an increase in local fluid shear force, which can be used for performing human physiological and pathological flow simulations for applications such as cell biology, disease modeling, and drug discovery, thus expanding fundamental insights into biology and medicine for researchers (*25*, *46*–*48*). μSonic-hand can directly stimulate controllable fluids at specific positions in 3D space, which is not available using microfluidic devices. It can enrich the application scenarios, especially for the differential treatment of cells or tissues in localized regions of interest. For example, fluid shear stimulation can create transient pores in cell membranes, facilitating drug delivery and gene therapy (Fig. 2C). To assess membrane permeability changes induced by the μSonic-hand, HeLa cells were immersed in propidium iodide (PI) solution (movie S2). A micropipette was positioned close to, but not touching, the cells, and real-time fluorescence imaging was recorded. Before activating the acoustic field ($t = 0$), no notable fluorescence was detected, indicating that PI did not cross the cell membrane. Upon activation, fluorescence intensity around the fluid shear region increased gradually, peaking at approximately 100 s, corresponding to the enhanced membrane permeability under fluid shear stimulation. Conversely, cells not exposed to the fluid shear exhibited no notable fluorescence throughout the experiment.

Harvesting specific cells in the liquid culture medium is a crucial procedure in biological research, typically achieved through flow cytometry sorting. A single cell with 10 to 30 μm near the micropipette end experiences a minor secondary acoustic radiation force due to the scattering of incident waves near the oscillating bubble. As shown in Fig. 2D, the strong drag force resulting from the streaming, coupled with a moderate secondary acoustic radiation force, confines the cells to a confined space proximate to the end of the micropipette. By moving the micropipette close to the substrate in the region of interest (ROI), more cells become entrapped and aggregate due to cell-cell adhesion forces, and the vortex field magnitude plays a dominant role in the final agglomerate size and the number of the trapped cells. Robotic movement of the micropipette enables the programable harvest of the selected cells by the μSonic-hand (fig. S6). The μSonic-hand packs the cells within the ROI into a cell cluster, which is subsequently transferred collectively using the micropipette. We validated this cell harvest strategy by carrying out experiments with fluorescently labeled cells. Experimental results show that most of the targeted cells were successfully collected, with collection rates of 79.2 and 83.6% for green and orange cells, respectively (fig. S7 and movie S2). Here, the fluorescence staining is only used to indicate the target cells, which is, in fact, not necessary. In contrast to flow cytometry sorting, cell harvest using the μSonic-hand is label free, hypotoxic, cost effective, and highly programmable. In contrast to harvesting cells by sucking target cells into the micropipette one by one, the μSonic-hand achieves much higher efficiency and prevents damage caused by friction with the micropipette's inner wall.

3D transportation via acoustic radiation force

The acoustic radiation force governs the trapping and transportation of the microobject using the proposed μSonic-hand (Fig. 3A). Initially, the micropipette end was positioned upward to the microsphere. By applying the appropriate input voltage and frequency to the piezoelectric transducers, the microspheres are immediately attracted by the resulting secondary acoustic radiation force. Last, under the joint action of gravity, acoustic wave, fluid dynamics, and multiple interfaces, all the forces were balanced when the microsphere was located at a specific position. Once trapped, the microsphere could be transported by μSonic-hand to any location in the fluidic environment along a programmed trajectory. During transportation, the streaming force on the object acts as a repulsive force, and the acoustic radiation effect generated by the incident waves scattering near the oscillating bubble provides the attractive force, together immobilizing the object in the immediate vicinity (without contact) of the micropipette end (fig. S8 and movie S3). Subsequently, switching off the acoustic field could result in the disappearance of the secondary radiation force and the immediate release of the microsphere.

The forces acting on the objects include secondary radiation force F_R, streaming drag force F_{SD}, gravity G, and buoyancy F_B. For objects such as PS and biological samples with densities slightly greater than the surrounding liquid, the difference between gravity and buoyancy can be expressed in terms of negative buoyancy $F_{NB} = G - F_B$, keeping the object at the lower part of the axisymmetric streaming. Although the trapping force can be calculated using the equation $\overrightarrow{F_T} = \overrightarrow{F_R} - \overrightarrow{F_{SD}} - \overrightarrow{F_{NB}}$, it is challenging to accurately resolve due to

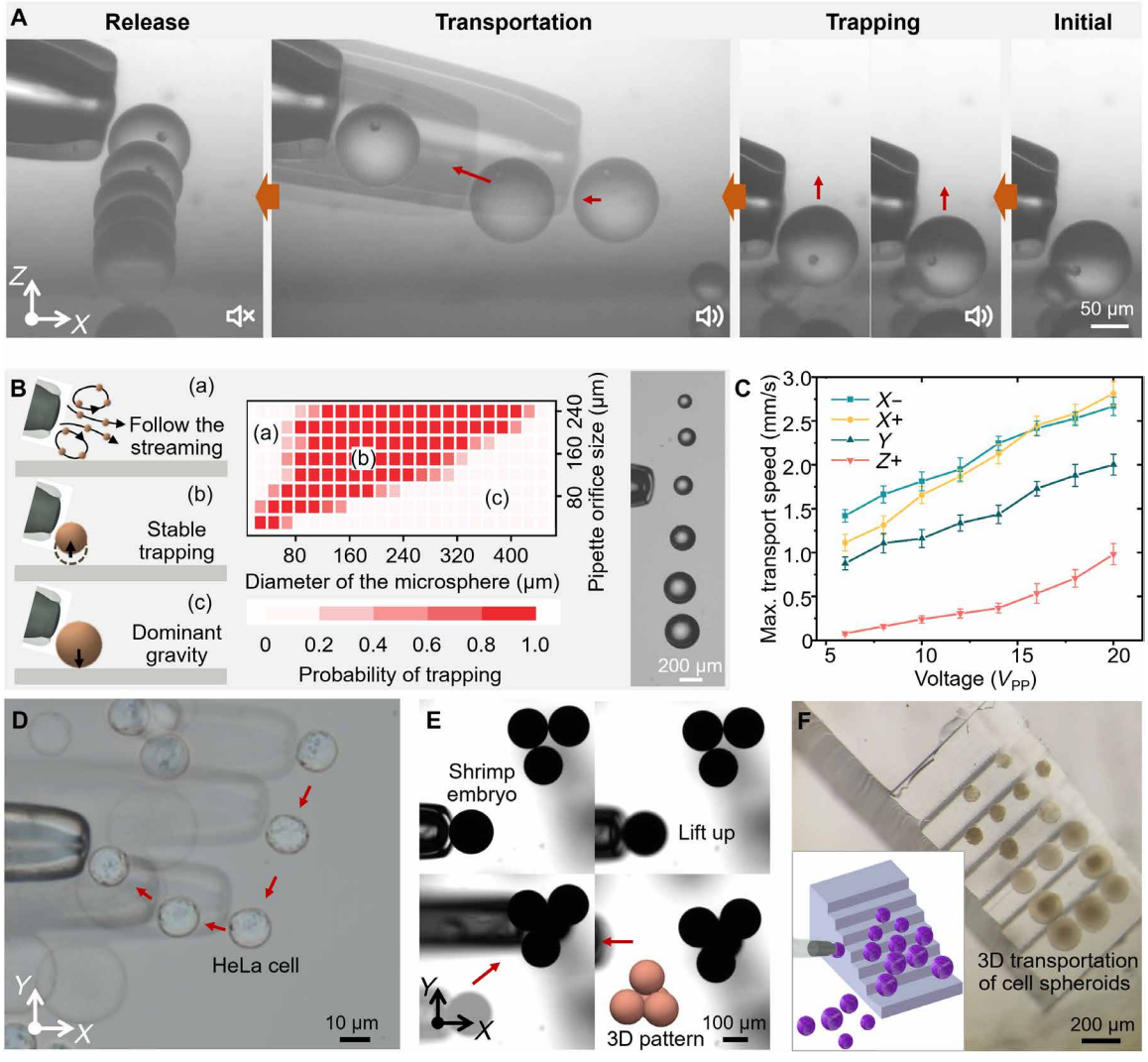

Fig. 3. 3D transportation via acoustic radiation force. (**A**) A continuous, complete process including trapping, transporting, and releasing operations of PS microspheres (from right to left). (**B**) Size range of the microspheres successfully trapped by micropipette with different orifice sizes: (a) undersized microspheres dominated by the drag force follow the streaming; (b) stable trapping of microsphere by the micropipette with appropriate orifice size; (c) failure in trapping oversized microspheres due to dominant gravitational forces. The graph shows the success rates of trapping microspheres of different sizes using micropipettes of different orifice sizes. The figure on the right demonstrates aligning PS microspheres with different sizes simultaneously using a single micropipette (movie S3). (**C**) The maximum transportation velocities in different directions are governed by the input voltage amplitudes (movie S3). (**D** to **F**) Use μSonic-hand to transport and pattern HeLa cells, shrimp eggs, and 3T3 cell spheres across ten to hundred micrometers in a 3D workspace, respectively (movie S3).

the difficulty in estimating the radiation force and streaming drag force. Predicting the precise location of the trapped object is also difficult, yet the object remained ultrastable at the balanced position due to minimal fluctuations of the individual forces. In experiments, we found that the diameter of the microspheres substantially affects the overall force state and, in particular, is an important factor in determining the size of the micropipettes. As shown in Fig. 3B, experiments with microspheres of varied diameters were conducted to investigate the one-time trap success rate as influenced by the sizes of the microspheres and the inner diameters of the micropipette orifices (movie S3). Micropipettes with orifices ranging from 30 to 240 μm were prepared. They were used five times to trap each PS microsphere, with diameters ranging from 20 to 420 μm, with the same input voltage of 5 V_{PP} (peak-to-peak voltage), and the success rates were recorded. Position fluctuations greater than the sphere's radius were considered failed traps. The gravity, buoyancy, and secondary acoustic radiation forces acting on the microspheres increase cubically with their diameter, whereas the fluid drag force scales linearly. Consequently, when the microspheres are too large relative to a given microbubble size, gravity becomes the dominant force, preventing successful trapping. Conversely, for microspheres that are too small, fluid resistance dominates, resulting in unstable immobilization or movement along the streamline. As the size of the micropipette and the contained bubble increases, the acoustic radiation force strengthens relative to the fluid drag force, enabling the trapping of larger microspheres and thus expanding the operational trapping range. PS microspheres of different sizes were simultaneously aligned in a single line using a single micropipette. This demonstration effectively highlights the cross-scale operational capability of the proposed μSonic-hand, a unique feature not now achievable with a single device.

To improve operation efficiency, the maximum transportation speed is an important indicator. As shown in Fig. 3C and movie S3, experiments revealed that the input voltage amplitude governs the maximum transportation velocity, which varies in different directions. The input voltage amplitude influences the magnitude of the secondary radiation force, and the direction of transportation determines the direction of the additional streaming drag force. In upward transportation, the velocity is much lower, primarily due to gravity causing the object to move away from the oscillating microbubble. However, we achieved transportation velocities of millimeters per second for a 100-μm microsphere using an 80-μm micropipette orifice in four selected directions (Fig. 3C), providing sufficient transportation efficiency for most applications. Benefiting from the stable and efficient transport of microobjects by μSonic-hand, we have demonstrated its 3D manipulation of microspheres, single cells, and microtissues, which is essential in many biomedical applications. As shown in Fig. 3 (D to F), the μSonic-hand was used to transport and pattern HeLa cells (Fig. 3D), shrimp eggs (Fig. 3E), fully automated transportation and alignment of microspheres (fig. S9), and 3T3 cell spheres (Fig. 3F) across ten to hundred micrometers in a 3D workspace, respectively (movie S3).

Multidirectional rotations in 3D axisymmetric streaming

Rotational motions are more ubiquitous throughout nature than translational motions, particularly at the microscale. The ability to rotate objects under the microscope frees researchers from the constraints of the 2D focal plane and facilitates the acquisition of 3D full-image information, minimizing the potential for erroneous conclusions from incomplete sample assessments. In single-cell operations, such as injection and nucleation, orientation control based on rotational operations is crucial for success, yet it still relies on a trial-and-error method (*15*, *49*). Controllable multidirectional 360° rotational operations are challenging to perform at the microscale. In this study, 360° rotational operations are achieved via controllable microstreaming induced by the proposed μSonic-hand. The rotation direction is controlled by finely adjusting the object's relative position in the 3D axisymmetric streaming, and the rotational velocity is easily regulated by the input voltage amplitude.

Figure 4A and fig. S10 show the streaming pattern influenced by the trapped microsphere. The rotational flow surrounding the object generates a torque that drives the object to rotate. In this setup, the rotation axis is perpendicular to the horizontal plane. Microspheres can also be positioned on the opposite side of the micropipette and rotate in the opposite direction (fig. S10), depending on their initial position in the streaming. The streaming pattern is symmetric along the micropipette axis (Figs. 1B and 4B), allowing control of the microsphere's rotation direction in all directions by adjusting its position relative to the micropipette's central axis. The position of the microsphere in the 3D axisymmetric streaming is controlled by moving the bubble-containing micropipette along the *z* axis. Using the boundary constraint on the induced streaming and the trapped object, moving the micropipette orifice close to the bottom substrate can force the trapped object to switch from position b to position a or c, while moving the micropipette orifice away from the bottom substrate allows the object to return to position b (Fig. 4B). When the trapped object is less dense than the fluid or subject to an upward fluid force, it will move to position d. Position d is rare in practical operations because it only occurs when the trapped object has a lower density than the fluid. Side views of the rotating microspheres at positions a and b demonstrate achieved rotations with different axes. Moreover, upon turning off the acoustic field, the low Reynolds number fluid rapidly ceases to flow. The rotating PS microsphere also immediately stops to sink to the bottom, which allows for the fine adjustment of the object's posture through on-off control. The stable rotation, rotation direction control, and on-off control are recorded in movie S4.

Manipulating cross-scale various biological samples

There is a notable current and potential demand for manipulating various small biological samples in biomedical operations and analysis, especially for rotational operations. Over the past decade, various methods have been developed to rotate specific biological objects, including rotating HeLa cells with optical tweezers (*50*), rotating zebrafish embryos with magnetic tweezers (*20*), rotating *Caenorhabditis elegans* using acoustic streaming in microchannels (*51*), and rotating mouse oocytes through microstreaming induced by vibration (*52*). Depending on the size, density, and other physical properties of the biological samples, as well as the operational environment, the appropriate driving force must be selected, and the tools must be well designed to rotate specific biological objects, presenting a notable challenge to biologists. A universal micromanipulation method capable of trapping, transporting, and rotating cross-scale various biological samples without restrictions on their physical properties could accelerate the development of biological research and medical treatment at the microscale.

As shown in Fig. 4C and movie S5, the proposed μSonic-hand can trap and rotate animal cells, plant cells, reproductive cells, single-celled organisms, embryos, and *C. elegans* across several micrometers to approximately 1 mm. In the process, the uneven microstreaming

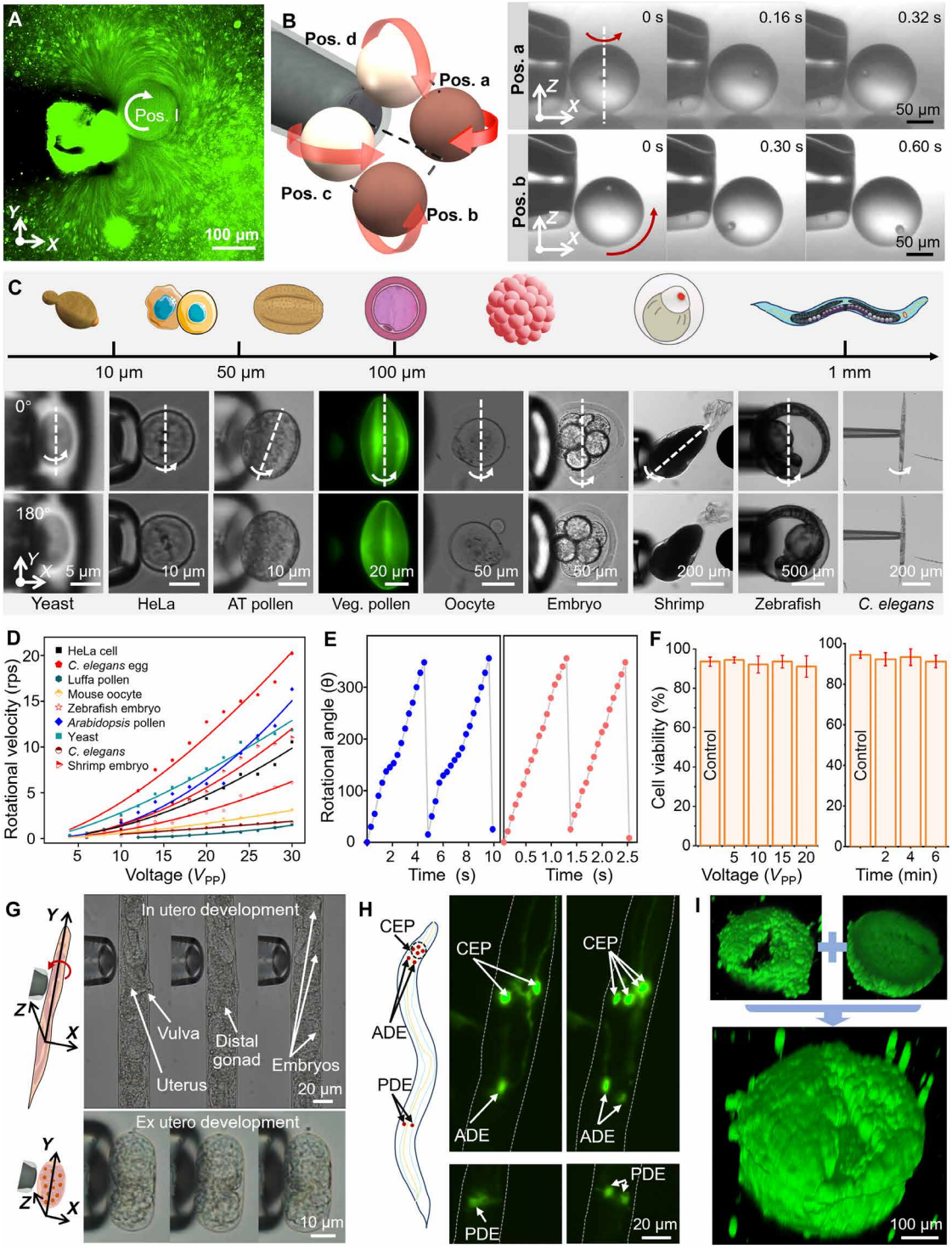

Fig. 4. Multidirectional rotations in 3D axisymmetric streaming and related applications. (**A**) Streaming around the trapped microspheres visualized by the 1-μm PS fluorescent particles (movie S4). Pos., position. (**B**) Multidirectional rotation by altering the object's relative position in the axisymmetric vortex (movie S4). The microsphere at positions a and b rotates along the *Z* axis and the *Y* axis, respectively. (**C**) The μSonic-hand traps and rotates yeast cells (~7 μm), HeLa cells (~20 μm), *A. thaliana* pollen (~30 μm), luffa pollen (~60 μm), mouse oocytes (~100 μm), mouse embryos (eight-cell stage, ~120 μm), shrimp eggs (~250 μm), zebrafish embryos (~1 mm), and *C. elegans* (~50 μm in diameter and 1 mm in length) (movie S5). AT, *A. thaliana*; Veg., luffa (vegetable) pollen. (**D**) Rotational velocity versus input voltage. (**E**) Rotation angle of mouse embryos and *A. thaliana* pollen over time. (**F**) Results of cell viability after μSonic-hand manipulation at different driving voltages and operating times. (**G**) 3D observation of *C. elegans* development by rotating their embryos from in utero to ex utero (movie S5). (**H**) Robust immobilization and controllable rotation of *C. elegans* (BZ555) allow direct observation of the dopaminergic neurons of interest from different directions (movie S5). CEP, cephalic; ADE, anterior deirid; PDE, posterior deirid. (**I**) Enhanced 3D images of a cell spheroid by integrating two images captured from 0° and 180° using a standard laser scanning confocal microscopy (LSCM) (movie S5).

force integrals form the torque acting on the object. Once the frequency is set, the input voltage amplitude becomes the only parameter that can control the streaming velocity. As shown in Fig. 4D, to investigate the relationship between the rotational velocity and the amplitude of the applied sinusoidal voltage, nine biological samples have been rotated under different peak-to-peak voltages. Experimental results show that the rotational velocity increases with the amplitude of the applied sinusoidal voltage.

In an aqueous environment, the streaming velocity u exhibits a quadratic relationship with the amplitude ε of the oscillating microbubble, which has a linear relationship with the input voltage V. Thus, the rotational velocity ω is proportional to the square of the voltage, $\omega \sim V^2$ (text S2). The data of rotational velocity versus input voltage were replotted in double logarithmic coordinates, and the slope was used to obtain the power function exponent, as illustrated in fig. S11. The slopes for HeLa cells, *C. elegans* eggs, luffa pollen, mouse oocyte, zebrafish embryos, *Arabidopsis thaliana* pollen, yeast, *C. elegans*, and shrimp embryos were 2.49, 2.37, 2.93, 1.52, 1.89, 2.05, 1.87, 1.40, and 2.28, respectively. While the experimental data clustered around 2, notable deviations remained. These deviations could be due to the irregular shapes, uneven mass distribution of the biological objects, and deformation of the soft biological membranes caused by the flow shear force. Furthermore, we assessed the angular velocity stability of the objects by continuously recording the rotation angle over time and obtained the rotation cycle, as depicted in Fig. 4E, which performed satisfactorily for both soft-textured embryos and small-sized *A. thaliana* pollen. The proposed μSonic-hand exhibits its excellent capability of operating multiscale objects, providing stable multidirectional 360° rotation and controllable rotational velocity, all essential for many microscale biomedical applications.

As described in Introduction, one of the main gains that can be expected from mechanical contact, light fields, electric fields, etc. to acoustic streaming is the absence of the deleterious effects. HeLa cell spheroids were used to assess the effect of μSonic-hand manipulation on cell viability. In Fig. 4F, the cell viabilities of the cells in the cell spheroids operated with varied input voltages and operational time were evaluated. The cell viabilities all exceeded 90% across all experimental conditions, demonstrating minimal cytotoxicity under the tested parameters (fig. S12). The maximum input voltage and operational time set in this experiment were smaller than those required for most acoustic micromanipulations, and within this range, cell viability did not decrease as the operational time or input voltage increased. This finding is consistent with previous research works about the acoustohydrodynamic micromanipulation (*25*, *46*–*48*). Moreover, the rotating cell spheroids are subjected to much less fluid shear stress (FSS) than the fixed cell adhering to the dish, because the relative velocity between the fluid and rotating object surface is much lower. As shown in Figs. 3C and 4D and table S2, the proposed μSonic-hand operates at a very low input voltage, enabling transportation and rotation of various cross-scale objects at sufficient velocities. This low-voltage operation minimizes potential adverse effects from FSS while supporting multiple functions.

Applications in 3D imaging under microscope

Constructing 3D morphologies of early embryonic development in *C. elegans* has been a focus of researchers, providing valuable data for developmental biology, cell biology, and biomechanics. Despite the relative transparency of *C. elegans*, obtaining comprehensive and clear information using a traditional optical microscope can be challenging, particularly for adult *C. elegans* with thick tissues. Precise and controlled rotation provides an efficient approach for rapidly acquiring high-resolution 3D models. However, most current methods depend on immobilizing *C. elegans* in microchannels, which complicates sample loading and collection, restricts access to other processes, and imposes strict size constraints on the nematodes. As shown in Fig. 4G, the proposed μSonic-hand enables multiangle observation of adult *C. elegans* and individual embryos, facilitating the analysis of embryonic development from early egg proliferation within the maternal body to organogenesis and morphogenesis in vitro. To clarify, *C. elegans* are initially treated with levamisole, a commonly used anesthetic for nematodes, to reduce physical activity during the process. In addition to embryonic development research, we also used the μSonic-hand to obtain the high-resolution multiview images of neurons in *C. elegans*. The BZ555 strain (*egls1 [dat-1p::GFP]*), which is commonly used to study Parkinson's disease and related treatments, has a total of eight dopaminergic neurons that are difficult to observe simultaneously under an optical microscope due to the overlapping of left-right or dorsal/ventral neuron pairs. As shown in Fig. 4H and movie S5, robust immobilization and controllable rotation by μSonic-hand allow direct observation of the neurons of interest from different directions.

Laser scanning confocal microscopy (LSCM) has been widely used for the 3D reconstruction of samples by overlaying optical sections. However, LSCM suffers from reduced fluorescence signal intensity and resolution in scanning thick and low-transparency samples. This is mainly due to the reduced excitation energy absorbed by the sample as the focus moves away from the coverslip and light scattering in penetrating the sample. The proposed μSonic-hand offers an affordable solution by rotating biological micro samples, allowing LSCM to scan samples from different directions and collect surface topography information. By piecing together these multiview images, a 3D model can be reconstructed. This approach markedly enhances the 3D imaging capabilities of LSCM in terms of spatial resolution and observation depth. Figure 4I and movie S5 demonstrate the enhanced 3D images of a cell spheroid by integrating two images captured from 0° and 180° using a standard LSCM equipped with the μSonic-hand.

Applications in embryo engineering

Recent advances in embryo engineering have greatly accelerated developments in life sciences and reproductive medicine, particularly in the areas of gene editing, cloning, and assisted reproduction (*5*). However, existing experimental processes in embryo engineering, including intracytoplasmic sperm injection (ICSI), preimplantation genetic diagnosis (PGD, also named embryo biopsy), and somatic cell nuclear transfer technologies, are suffering from disappointingly low success rates and lack of experienced embryologists. Recently, despite direct mechanical contact, more physical interaction ways have been applied to renew the manipulation of the oocytes and embryos in embryo engineering (*53*). However, few biologists or physicians are adopting these recently developed micromanipulation methods in their practices because the complex device requirement attributes of these physical fields make them difficult to deploy directly on existing general-purpose micromanipulation platforms in laboratories or hospitals, and the singularity of functionality does not satisfy clinical needs. Moreover, these additional devices, such as microchannels and narrow workspace of the electromagnetic coils, may hinder access to other tools and operations, and optical or electric fields may damage the valuable oocytes and embryos. The proposed

μSonic-hand can markedly improve the manipulation of oocytes and embryos using noninvasive acoustic gas-liquid-solid interactions, enabling the required multifunctional micromanipulation while minimally modifying the standard cell injection setup in biomedical laboratories. Only a piezoelectric transducer is required to be adhered under the petri dish.

In the ICSI, as shown in Fig. 5A, the embryologist should directly inject the sperm into a selected healthy oocyte. Essential operations include immobilization, transportation, and 3D reorientation. The oocytes must be classified first, and then the selected healthy ones should positioned and immobilized at the desired injection position. In addition, out-of-plane rotation is required to bring the internal polar body into the focal plane, followed by in-plane rotation to place the polar body at the 12 or 6 o'clock position, away from the penetration site. Classifying oocytes to select healthy ones, achieving the desired posture through 3D reorientation, shortening operational time, and minimizing frequent mechanical contact can markedly improve the success rate of embryo formation. Now, embryologists commonly transport oocytes by aspiration and reorient them by applying positive and negative pressure alternately, a typical trial-and-error approach featuring extremely low efficiency and considerable damage. Here, the proposed μSonic-hand provides a noninvasive multifunctional approach for classifying, arraying, and 3D reorientation, covering almost all the critical processes in the ICSI. In addition, the μSonic-hand can rotate the early-stage embryo obtained by the ICSI, providing multiview images for 3D morphological evaluation and grading.

Before applying the proposed μSonic-hand in the ICSI for assisted reproduction, we performed a series of experiments using mouse oocytes and early embryos for classification, transportation, and alignment. In addition, we rotated and observed the mouse embryos from all angles to monitor early embryonic development in the long term and performed 3D reorientation of the early-stage embryo for mouse embryo biopsy (Fig. 5, B to E, and movie S6). As shown in Fig 5B, a selected healthy mouse oocyte was trapped and transported to the desired position by the μSonic-hand, and nine healthy oocytes were arrayed regularly under the microscope within 26 s. Subsequently, an oocyte was reoriented by out-of-plane rotation until the polar body (arrowed in Fig. 5C) appeared in the visual field. Through subsequent in-plane rotation, the polar body was positioned at the 12 o'clock direction. Last, the sperm was injected into the mouse oocyte immobilized by the micropipette with negative pressure. During the entire injection process, mechanical contact only occurs once in the final injection, minimizing potential damages. In addition, detection of embryonic division errors, embryo fragmentation in 3D space, and genetic abnormalities before implantation can help select healthy early embryos for implantation. We used μSonic-hand to rotate the early embryos to obtain multiview images for long-term 3D morphological monitoring and grading (Fig. 5D) and reoriented the embryos to achieve an appropriate posture for mouse embryo biopsy (Fig. 5E). Compared to the observation by cumbersome manual rotation of the embryos in clinic, optical sections obtained by the desk incubator equipped with an inverted microscope and 3D morphology obtained by confocal microscope in research suffer from optical occlusion and unstable trapping. μSonic-hand provides stable immobilization, controllable rotation to overcome optical occlusion, and potential high-resolution 3D morphology by combination with optical coherence tomography in the long-term 3D morphological monitoring of early embryonic development (table S3).

Experiments involving the manipulation of oocytes and early-stage embryos from mice demonstrate the potential of the proposed μSonic-hand in assisted reproduction. In assisted reproduction laboratories, oocytes and early-stage embryos formed through in vitro fertilization (IVF) that are of low quality and unsuitable for IVF or implantation should be discarded. With patient consent, we obtained discarded unhealthy oocytes and early-stage embryos from an assisted reproduction laboratory at a hospital in Beijing. As shown in fig. S3, we deployed the proposed μSonic-hand by simply including an additional $1 piezoelectric transducer in their cell injection set (RI Integra, UK). We carried out ICSI, PGD, long-term monitoring of early-stage embryos from multiple angles, and 3D morphological reconstruction of early-stage embryos using the proposed μSonic-hand (movie S6). All experiments were performed by embryologists after brief training. All samples were discarded following standard procedures after the experiments. As shown in Fig. 5 (F and G), a human oocyte was trapped, transported to the visual field center, and reoriented to the desired posture for the final injection. These operations and the injection took approximately 32 s, much less than the 2 min typically required by a well-trained embryologist. The experiments used a standard cell injection setup (Research Instruments, Integra 2) under an inverted microscope (Nikon, Ti2-E), with an additional piezoelectric transducer attached under the petri dish to generate an acoustic wave. The μSonic-hand also facilitated PGD through 3D reorientation during biopsies of early-stage human embryos (Fig. 5H). Moreover, early-stage embryos were rotated to observe them from all angles, allowing long-term 3D morphological monitoring during early embryonic development. Among the multiview images of developing early-stage embryos, only some revealed abnormal embryonic cell morphology and fragmentation in 3D space, highlighting the necessity of multiangle observation. In addition, with the aid of computer vision, we reconstructed the 3D morphology of an early-stage embryo from captured multiview images, enabling counting the number of embryonic cells, monitoring cell division, and detecting division errors at early developmental stages (Fig. 5I). This capability is rarely achieved by traditional 3D reconstruction methods based on optical sections. The experimental results demonstrate the great potential of the proposed μSonic-hand in mammalian embryo engineering.

DISCUSSION

In this work, we propose a versatile acoustohydrodynamic micromanipulation method, named μSonic-hand, driven by acoustic gas-liquid-solid interactions, for biomedical applications. In recent years, there have been many micromanipulation methods using mechanical, optical, electric, magnetic, and fluidic forces to transport and rotate objects at the micro-/milliscale. As shown in table S1, in the comparison between the proposed μSonic-hand and the recent advanced micromanipulation methods, we can observe its three important advantages, including the wide-range capabilities of operating both liquids and individual entities across scales and modalities, inherent biocompatibility brought by the acoustohydrodynamics, and extremely low cost of including an additional $1 piezoelectric transducer in a typical micromanipulation system.

The most important potential that the proposed μSonic-hand offers is the wide range of capabilities. This versatility can be divided into two main aspects: one is the multifunctional operations of both liquids and individual entities including mixing, dispersion, enhancing

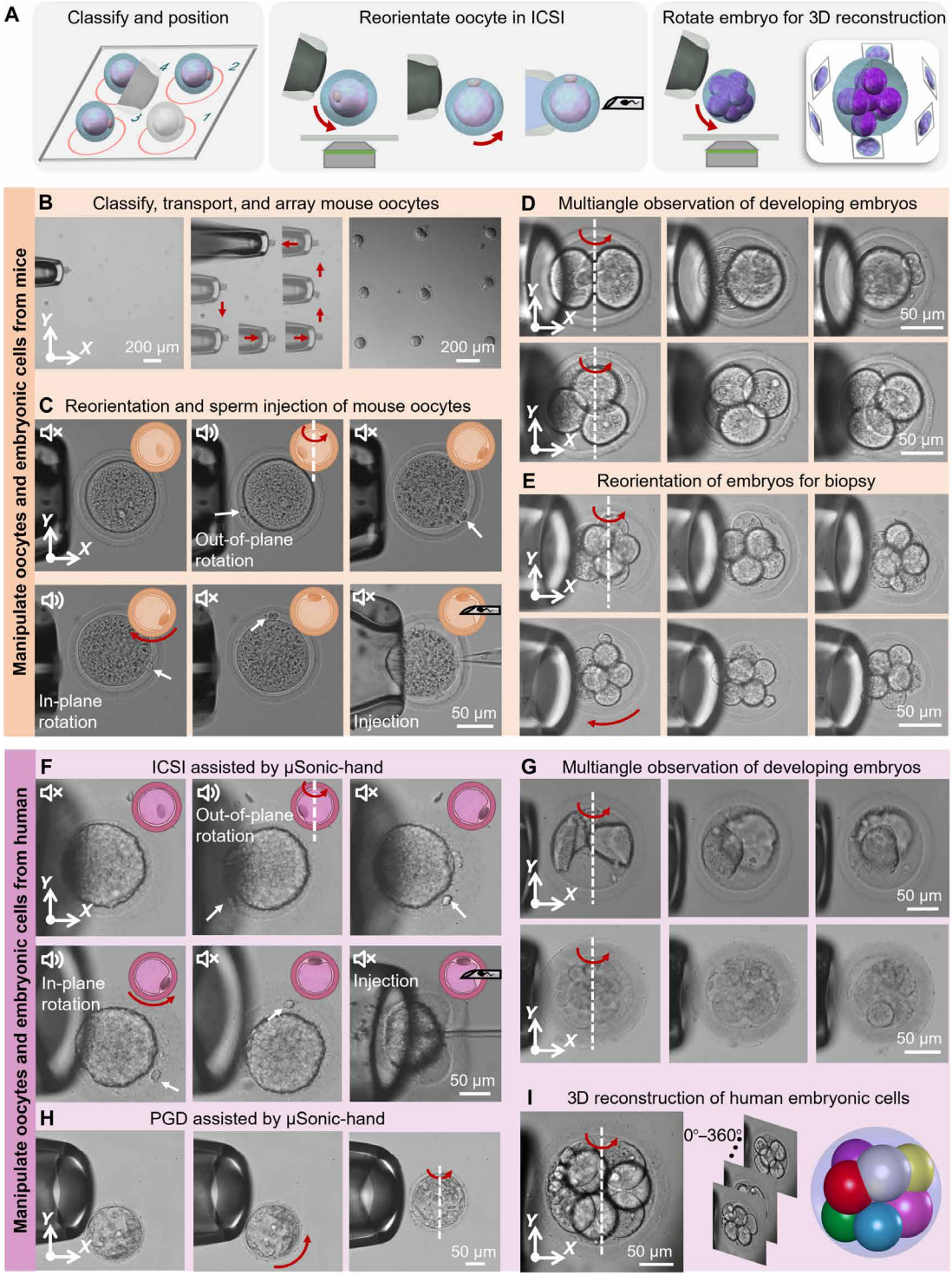

Fig. 5. Applications in embryo engineering. (**A**) Apply the μSonic-hand in the manipulation of oocytes and embryos, enabling the required multifunctional micromanipulation while minimally modifying the standard cell injection setup in biomedical laboratories. (**B**) Classify, transport, and array mouse oocytes in sample preparation. (**C**) Reorientation of mouse oocyte before injection. The polar body in the oocyte is arrowed. (**D**) Multiangle observation of developing mouse embryos, including two- and four-cell stages. (**E**) Reorientation of mouse embryo for biopsy. (**F**) ICSI assisted by μSonic-hand. The polar body in the human oocyte is arrowed. (**G**) Multiangle observation of developing human embryos, including two- and four-cell stages. (**H**) PGD assisted by μSonic-hand. (**I**) 3D reconstruction of human embryonic cells at the eight-cell stage (movie S6).

cell membrane permeability, harvesting target cells from the culture medium, stable trapping, rapid transportation, and multidirectional rotation; the other one is capabilities of operating yeast cells (~7 μm), HeLa cells (~20 μm), *A. thaliana* pollen (~30 μm), luffa pollen (~60 μm), mouse oocytes (~100 μm), mouse embryos (eight-cell stage, ~120 μm), shrimp eggs (~250 μm), and zebrafish embryos (~1 mm) ranging from micrometers to millimeters. In contrast, micromanipulation driven by electric, magnetic, and optical field forces is heavily reliant on the specific physical and structural properties of the objects being manipulated, rendering them unsuitable for a diverse range of cross-scale objects (*18*–*21*, *54*). Compared with microfluidic chips, the proposed μSonic-hand induces microstreaming in an open environment, allowing more convenient integration of other functional units and operation of cross-scale objects with more degrees of freedom. Most existing acoustohydrodynamic micromanipulation methods are also performed in microfluidic chips, using the confinement of the microchannel to optimize its low controllability. Although the combination of acoustic driving and microfluidic chips brings more functions, the inherent disadvantages of the microfluidic chips caused by the closed environment and inner fixed geometries remain. Controllable precise single-cell operation, 3D cross-plane transportation, and multidirectional rotation of the proposed μSonic-hand are the main improvements of the existing acoustic micromanipulation methods.

The most unique feature of the proposed μSonic-hand is the extremely low cost. By including an additional $1 piezoelectric transducer in a universal micromanipulation system, it gains the abovementioned capabilities. The proposed μSonic-hand renews the interaction method without largely altering commonly used micromanipulation setups or the experimental processes in biomedical laboratories. For instance, when we finish the 3D reorientation of the oocytes, the injection process follows seamlessly. The main reason is that the proposed μSonic-hand modifies the existing cell injection system and the oocyte injection procedure little with an extremely low cost. Applications in 3D imaging under microscope and embryo engineering demonstrate that the proposed low-cost micropipette-based micromanipulation method can be rapidly deployed in biomedical laboratories for complex microscale operations and analyses. In contrast, other micromanipulation systems that use optical, electric, magnetic fields, and microfluidic chips require precision light sources, microelectrode arrays, high-power electromagnetic coils, and precise pumps, respectively, which are relatively more complex and expensive. Moreover, the conventional experimental procedures need to be renewed to adapt to the micromanipulation method driven by these field forces (*4*, *5*, *12*, *17*).

At last, the inherent biocompatibility of the proposed μSonic-hand is the most necessary feature for biomedical applications. Over the past few decades, electric, magnetic, and optical field forces have been used to drive the micromanipulation of biological objects. However, potential damage resulting from direct illumination with intense lasers, the heating effects of electric fields, and the inclusion of external magnetic materials further limit their application in manipulating living biological samples (*15*). The proposed μSonic-hand, based on acoustohydrodynamics, emerges as a promising innovative micromanipulation method for operating liquids and individual entities at the microscale in biomedical applications, offering inherent high biocompatibility. The proposed μSonic-hand is based on acoustically driven gas-liquid-solid interactions. Stimulated by a piezoelectric transducer, the oscillating gas-liquid interface generates controllable acoustic microstreaming with a defined pattern. Neither the acoustic fields nor the generated acoustic streaming will damage the operated biological objects. The experimental results analyzing the viability of cells within the cell spheroids operated by the μSonic-hand clearly demonstrate that the μSonic-hand has not caused any observable damage.

The experiments conducted in our study have demonstrated that the proposed μSonic-hand features wide-range capabilities, inherent biocompatibility, and an extremely low cost. The enhancement of microfluidic mass transfer can be applied to efficient solid reagent dissolution, on-demand chemical reactions, cell transfection, and cell lysis through high shear forces. The micromanipulation of individual entities also has important applications in the local characterization of single cells and microassembly-based bottom-up tissue engineering (*55*). By leveraging the deep penetration capability of acoustic waves, we envision that the proposed μSonic-hand could facilitate in vivo manipulation within the fluidic environment of the human body.

MATERIALS AND METHODS

Experimental setup

The multifunctional biological micromanipulation system illustrated in Fig. 1 and fig. S1 is built upon an inverted microscope (Eclipse Ti2-E, Nikon, Japan). The μSonic-hand micropipette and objects are monitored, while vision-based mission planning and motion control are facilitated by a scientific complementary metal-oxide semiconductor camera (edge 4.2 LT, PCO, Germany). A confocal laser scanning microscope (C2, Nikon, Japan) is mounted on the left side of the microscope for imaging tasks. A piezoelectric transducer emits acoustic waves, with its signal generated by a function generator (AFG-2225, GW Instek); signal amplification is performed, if necessary, using a voltage amplifier (ATA-2022H, Aigtek, China). The piezoelectric transducer is bonded to a glass slide and secured to a hot plate on the carrier table for temperature adjustment. A 3D motorized precision stage (stick-slip piezo XYZ stage, SLS-3232, SmarAct, Germany) is fixed to the optical microscope mount to enable spatial positioning of the micropipette. The micropipette itself is mounted on an injection holder (HI-9, Narishige, Japan), and the position of the gas-liquid interface of the microbubbles is adjusted using pressure pumps (FLOW EZ, Fluigent, France).

Preparation of micropipettes

The manufacturing process of micropipettes for carrying bubbles is shown schematically in fig. S13. First, the glass micropipette is subjected to heat and pulled into two halves with the help of a needle puller (PC-100, Narishige). One of the halves is chosen, and the orifice is ground to the desired size using a microgrinder (EG-402, Narishige), or, in the case of larger size requirements, it may be trimmed using a microforce (MF-900) before grinding. Subsequently, the end tip is cleaned and positioned in close proximity to the heating bead on the microforce, where it is melted and deformed to the desired concave orifice. Analysis of the impact of the air-liquid interface curvature on the induced microstreaming pattern and operation is presented in text S5 and fig. S15. The preparation of the micropipettes in this work is very similar to the fabrication of holding pipettes in cell injection, and the commercialized holding pipette with the concave orifice can perform the proposed micromanipulation.

Quantify mixing efficiency

To quantitatively examine and evaluate the mixing efficiency, the mixing index was calculated using the following equation

$$\begin{cases} M_k = 1 - \dfrac{V_k}{V_0} \\ V_k = \dfrac{\sqrt{\frac{1}{n}\sum\left(C_i - C_m\right)^2}}{C_m} \end{cases}$$

where M_k is the mixing efficiency at moment k, V is the coefficient of variation, V_0 is the initial moment, C_i is the grayscale value of each pixel, C_m is the average value, and n is the total number of pixels. With this definition, the calculation results in 0 for no mixing and 1 for complete mixing.

Preparation of biosamples and microparticles

Yeast cells

The yeast cell suspension was prepared by adding 0.1 g of yeast cells (Angel Yeast Co. Ltd., China) to 100 ml of 0.9% sterile sodium chloride solution and thoroughly stirring, followed by aspirating the liquid near the bottom of the suspension during use.

Mammalian cells

The human cervical cancer HeLa cells and the human embryonic kidney (HEK) 293T cells were purchased from the American Type Culture Collection (USA). These cells were incubated in Dulbecco's modified Eagle's medium (DMEM) mixed with 10% fetal bovine serum (Invitrogen), penicillin (100 U/ml), and streptomycin (100 μg/ml) in an incubator (5% CO_2, 95% humidity, and 37°C). Single-cell suspensions were obtained using trypsin and then centrifuged and resuspended in DMEM at a density of 1×10^6 cells/ml.

Pollens

Stamens were cut from fresh plants of *A. thaliana* and luffa and then placed in Eppendorf tubes containing growth medium (for *A. thaliana*) and mineral oil (for luffa), respectively. Under the action of a vortex oscillator, pollen grains were released and immersed in the liquid. The bottom-clear suspension was taken after centrifugation. The composition of the *A. thaliana* pollen growth medium was as follows: 5 mM $CaCl_2$, 5 mM KCl, 1.6 mM H_3BO_3, 1 mM $MgSO_4$, 10% sucrose, and 1% low melting agarose at pH 7.5.

Cell spheroids

The 3D HEK 293T cell spheroids were prepared as mainly described in the previous study. Briefly, each well was preloaded with 100 μl of 1.5% sterile agarose solutions before seeding every 3000 cells into each well of 96-well plates. The medium is changed every 2 days, and the formation of 3D cell spheres is monitored with a universal optical microscope. The desired size of cell spheres can be harvested at any time during their growth. Fluorescent labeling of cell spheres was performed using calcein-AM and PI staining (04511, Sigma-Aldrich, USA) to assess the effect of the proposed method on cell viability.

Mouse oocytes and embryo collection

Six-week-old female C57BL/6 mice from Vital River Laboratory Animal Technology Co. Ltd. (Beijing, China) were maintained in cages undergoing at least three 12-hour light-dark cycles. Briefly, female mice were superovulated by injecting intraperitoneally of 10 IU of pregnant mare serum gonadotropin (P9970, Solarbio, China) at 6 p.m. on the first day and 10 IU of human chorionic gonadotropin (YZ-150513, Solarbio, China) at 6 p.m. on the third day. After mating one female with an 8- to 10-week-old male of the same strain, mice were euthanized at 8 a.m. on the fourth day. Cumulus-oocyte complexes from oviducts were collected into M2 culture medium (M7167, Sigma-Aldrich, USA), and cumulus cells were removed in hyaluronidase (H4272, Sigma-Aldrich, USA) and then washed in M2 culture medium. The oocytes were placed in an M16 medium (M7292, Sigma-Aldrich, USA) at 37°C with 6% CO_2 and incubated until use. Fertilized eggs were cultured in potassium simplex optimization medium (KSOM) medium (MR121, Sigma-Aldrich, USA) at 37°C with 6% CO_2, and embryos were collected at various stages of maturation. All experiments were approved by the Experimental Animal Protection and Ethics Committee of our university (approval number IACUC-AP-2024031216).

Human embryo source: The use of discarded human oocytes and embryos in this research adheres to the Human Biomedical Research Ethics Guidelines set by the National Health Commission of the People's Republic of China on 1 December 2016. The study's aims and protocols have been reviewed and approved by the local ethics committee of Beijing Chao-Yang Hospital (approval number 2022-1-4-1), Capital Medical University. Two MI-stage oocytes and four embryos (at the two-cell, four-cell, eight-cell, and blastocyst stages) used in this study were obtained from the Medical Center for Human Reproduction of Beijing Chaoyang Hospital, Capital Medical University (Beijing, China). Written informed consent was obtained from the patients.

C. elegans

In this study, the wild-type Bristol N2 and its eggs, as well as the transgenic strain BZ555 (P*dat-1::GFP*; bright GFP observable in dopamine neuronal soma and processes), were tested using the μSonic-hand. These strains were provided by the Beijing University of Chinese Medicine. They were maintained on agar plates containing nematode growth medium (NGM) at 20°C. The customized agar was prepared as follows: 3 g of NaCl, 2.36 g of KCl, 2.5 g of peptone, and 18 g of agar were dissolved in 975 ml of distilled water and autoclaved for 1 hour. When the temperature of the autoclaved mixture was reduced to 55°C, it was mixed with 1 ml of 1 M $CaCl_2$, 1 ml of 1 M $MgSO_4$, 1 ml of cholesterol (10 mg/ml), and 5 ml of mycotoxin (1.25 mg/ml) to obtain the final NGM agar plates. Bacterial food *Escherichia coli* OP50-1 was seeded within 24 hours.

To enable precise manipulation and observation of *C. elegans* using the μSonic-hand, it is necessary to paralyze and rigidify them via levamisole treatment. The preparation of M9 buffer is the first step: dissolve 3 g of KH_2PO_4, 6 g of Na_2HPO_4, and 5 g of NaCl in 1 liter of distilled water, autoclave, and cool. Afterward, add 1 ml of autoclaved 1 M $MgSO_4$ to complete the M9 buffer formulation. Levamisole solution with a concentration of 0.6 mg/ml is then prepared using this buffer. Before the experiment, *C. elegans* should be immersed in the paralyzing solution for 30 min, a condition that causes no notable harm at this concentration.

Brine shrimp embryo (Artemia salina)

Brine shrimp embryos were purchased from Bessn Feed Co. Ltd. (Shandong, China). Hatching is carried out at 25°C (pH 8.6) in 3.0% artificial synthetic seawater with continuous illumination and aeration. Sixteen hours later, those in the hatching stage and with complete exfoliation are collected.

Zebrafish embryos

Zebrafish embryos were prepared according to standard procedures (BioFish Inc., China). Because no destructive experiments were performed on zebrafish embryos in this study, development

could continue after the experiment until hatching. All experiments were approved by the Experimental Animal Protection and Ethics Committee of Beijing Institute of Technology.

PS microspheres

Three types of PS microspheres were used in our work. The suspension containing monodisperse PS microspheres with a diameter of 1 μm was purchased from BaseLine, Tianjin, China, which has a green fluorescent marker for microstreaming observation, and the suspension needs to be diluted to 0.2% (w/v) with pure water with shaking for mixing well before use. PS microspheres (Duke Scientific, USA), 5 to 500 μm in diameter and 1.05 g/cm^3 in density, were diluted with pure water to the desired concentration. Using the proposed method, they were subjected to micromanipulation experiments, including transport and rotation.

Nanoparticles

In the experiments of particle dispersion, Fe_3O_4 particles with a diameter of 500 nm without any treatment were placed in 10 ml of pure water to form a 1% (w/v) suspension, which was used after full immersion.

Supplementary Materials

The PDF file includes:

Supplementary Text
Figs. S1 to S15
Tables S1 to S3
Legends for movies S1 to S6
References

Other Supplementary Material for this manuscript includes the following:

Movies S1 to S6

REFERENCES AND NOTES

1. T. Fukuda, M. Fujiyoshi, F. Arai, H. Matsuura, "Design and dextrous control of micromanipulator with 6 DOF" in *Proceedings of the 1991 IEEE International Conference on Robotics and Automation* (IEEE, 1991), pp. 1628–1633.
2. Y. Sun, B. J. Nelson, Biological cell injection using an autonomous microrobotic system. *Int. J. Robot. Res.* **21**, 861–868 (2002).
3. A. Ozcelik, J. Rufo, F. Guo, Y. Gu, P. Li, J. Lata, T. J. Huang, Acoustic tweezers for the life sciences. *Nat. Methods* **15**, 1021–1028 (2018).
4. Z. Zhang, X. Wang, J. Liu, C. Dai, Y. Sun, Robotic micromanipulation: Fundamentals and applications. *Annu. Rev. Control. Robot. Auton. Syst.* **2**, 181–203 (2019).
5. Y. Ma, M. Gu, L. Chen, H. Shen, Y. Pan, Y. Pang, S. Miao, R. Tong, H. Huang, Y. Zhu, L. Sun, Recent advances in critical nodes of embryo engineering technology. *Theranostics* **11**, 7391–7424 (2021).
6. Q. Wang, K. F. Chan, K. Schweizer, X. Du, D. Jin, S. C. H. Yu, B. J. Nelson, L. Zhang, Ultrasound Doppler-guided real-time navigation of a magnetic microswarm for active endovascular delivery. *Sci. Adv.* **7**, eabe5914 (2021).
7. P. Liu, Z. Tian, K. Yang, T. D. Naquin, N. Hao, H. Huang, J. Chen, Q. Ma, H. Bachman, P. Zhang, X. Xu, J. Hu, T. J. Huang, Acoustofluidic black holes for multifunctional in-droplet particle manipulation. *Sci. Adv.* **8**, eabm2592 (2022).
8. P. Zhang, H. Bachman, A. Ozcelik, T. J. Huang, Acoustic microfluidics. *Ann. Rev. Anal. Chem.* **13**, 17–43 (2020).
9. A. Aghakhani, A. Pena-Francesch, U. Bozuyuk, H. Cetin, P. Wrede, M. Sitti, High shear rate propulsion of acoustic microrobots in complex biological fluids. *Sci. Adv.* **8**, eabm5126 (2022).
10. A. Marzo, B. W. Drinkwater, Holographic acoustic tweezers. *Proc. Natl. Acad. Sci. U.S.A.* **116**, 84–89 (2019).
11. H. Xie, M. Sun, X. Fan, Z. Lin, W. Chen, L. Wang, L. Dong, Q. He, Reconfigurable magnetic microrobot swarm: Multimode transformation, locomotion, and manipulation. *Sci. Robot.* **4**, eaav8006 (2019).
12. L. Zheng, Y. Jia, D. Dong, W. Lam, D. Li, H. Ji, D. Sun, 3D navigation control of untethered magnetic microrobot in centimeter-scale workspace based on field-of-view tracking scheme. *IEEE Trans. Robot.* **38**, 1583–1598 (2022).
13. H. Xie, H. Zhang, J. Song, X. Meng, Y. Wen, L. Sun, High-precision automated micromanipulation and adhesive microbonding with cantilevered micropipette probes in the dynamic probing mode. *IEEE/ASME Trans. Mechatron.* **23**, 1425–1435 (2018).
14. T. Tang, Y. Hosokawa, T. Hayakawa, Y. Tanaka, W. Li, M. Li, Y. Yalikun, Rotation of biological cells: Fundamentals and applications. *Engineering* **10**, 110–126 (2022).
15. C. Dai, Z. Zhang, Y. Lu, G. Shan, X. Wang, Q. Zhao, C. Ru, Y. Sun, Robotic manipulation of deformable cells for orientation control. *IEEE Trans. Robot.* **36**, 271–283 (2020).
16. T. Tanikawa, T. Arai, Development of a micro-manipulation system having a two-fingered micro-hand. *IEEE Trans. Robot. Automat.* **15**, 152–162 (1999).
17. A. Billard, D. Kragic, Trends and challenges in robot manipulation. *Science* **364**, eaat8414 (2019).
18. L. Paterson, M. P. MacDonald, J. Arlt, W. Sibbett, P. E. Bryant, K. Dholakia, Controlled rotation of optically trapped microscopic particles. *Science* **292**, 912–914 (2001).
19. U. Bozuyuk, A. Aghakhani, Y. Alapan, M. Yunusa, P. Wrede, M. Sitti, Reduced rotational flows enable the translation of surface-rolling microrobots in confined spaces. *Nat. Commun.* **13**, 6289 (2022).
20. F. Berndt, G. Shah, R. M. Power, J. Brugués, J. Huisken, Dynamic and non-contact 3D sample rotation for microscopy. *Nat. Commun.* **9**, 5025 (2018).
21. L. Huang, P. Zhao, W. Wang, 3D cell electrorotation and imaging for measuring multiple cellular biophysical properties. *Lab Chip* **18**, 2359–2368 (2018).
22. Z. Chen, J. Li, Y. Zheng, Heat-mediated optical manipulation. *Chem. Rev.* **122**, 3122–3179 (2022).
23. Y. Bhosale, G. Vishwanathan, G. Upadhyay, T. Parthasarathy, G. Juarez, M. Gazzola, Multicurvature viscous streaming: Flow topology and particle manipulation. *Proc. Natl. Acad. Sci. U.S.A.* **119**, e2120538119 (2022).
24. A. Shenoy, C. V. Rao, C. M. Schroeder, Stokes trap for multiplexed particle manipulation and assembly using fluidics. *Proc. Natl. Acad. Sci. U.S.A.* **113**, 3976–3981 (2016).
25. M. Urbanska, H. E. Muñoz, O. Otto, J. Shaw Bagnall, S. R. Manalis, D. Di Carlo, J. Guck, A comparison of microfluidic methods for high-throughput cell deformability measurements. *Nat. Methods* **17**, 587–593 (2020).
26. L. Feng, S. Liang, X. Zhou, J. Yang, Y. Jiang, D. Zhang, F. Arai, On-chip microfluid induced by oscillation of microrobot for noncontact cell transportation. *Appl. Phys. Lett.* **111**, 203703 (2017).
27. X. Tang, X. Liu, P. Li, F. Liu, M. Kojima, Q. Huang, T. Arai, On-chip cell–cell interaction monitoring at single-cell level by efficient immobilization of multiple cells in adjustable quantities. *Anal. Chem.* **92**, 11607–11616 (2020).
28. Y. Gu, C. Chen, J. Rufo, C. Shen, Z. Wang, P.-H. Huang, H. Fu, P. Zhang, S. A. Cummer, Z. Tian, T. J. Huang, Acoustofluidic holography for micro- to nanoscale particle manipulation. *ACS Nano* **14**, 14635–14645 (2020).
29. W. S. Harley, K. Kolesnik, M. Xu, D. E. Heath, D. J. Collins, 3D acoustofluidics via sub-wavelength micro-resonators. *Adv. Funct. Mater.* **33**, 2211422 (2023).
30. S. Kim, H. Nam, B. Cha, J. Park, H. J. Sung, J. S. Jeon, Acoustofluidic stimulation of functional immune cells in a microreactor. *Adv. Sci.* **9**, 2105809 (2022).
31. A. Pourabed, J. Brenker, T. Younas, L. He, T. Alan, A lotus shaped acoustofluidic mixer: High throughput homogenisation of liquids in 2 ms using hydrodynamically coupled resonators. *Ultrason. Sonochem.* **83**, 105936 (2022).
32. N. F. Läubli, J. T. Burri, J. Marquard, H. Vogler, G. Mosca, N. Vertti-Quintero, N. Shamsudhin, A. DeMello, U. Grossniklaus, D. Ahmed, 3D mechanical characterization of single cells and small organisms using acoustic manipulation and force microscopy. *Nat. Commun.* **12**, 2583 (2021).
33. X. Liu, Q. Shi, Y. Lin, M. Kojima, Y. Mae, T. Fukuda, Q. Huang, T. Arai, Multifunctional noncontact micromanipulation using whirling flow generated by vibrating a single piezo actuator. *Small* **15**, 1804421 (2019).
34. J. Durrer, P. Agrawal, A. Ozgul, S. C. F. Neuhauss, N. Nama, D. Ahmed, A robot-assisted acoustofluidic end effector. *Nat. Commun.* **13**, 6370 (2022).
35. P. Marmottant, S. Hilgenfeldt, Controlled vesicle deformation and lysis by single oscillating bubbles. *Nature* **423**, 153–156 (2003).
36. M.De Corato, V. Garbin, Capillary interactions between dynamically forced particles adsorbed at a planar interface and on a bubble. *J. Fluid Mech.* **847**, 71–92 (2018).
37. K. Fung, S. Fan, T. J. Kolibaba, B. W. Caplins, J. P. Killgore, X. Ding, Y. Ding, 3D printed helmholtz microstreaming structures: Analysis of bubble dynamics, bulk fluid disturbance, and resiliency in nonquiescent conditions. *ACS ES T Water* **4**, 1741–1750 (2024).
38. A. Aghakhani, O. Yasa, P. Wrede, M. Sitti, Acoustically powered surface-slipping mobile microrobots. *Proc. Natl. Acad. Sci. U.S.A.* **117**, 3469–3477 (2020).
39. J. Janiak, Y. Li, Y. Ferry, A. A. Doinikov, D. Ahmed, Acoustic microbubble propulsion, train-like assembly and cargo transport. *Nat. Commun.* **14**, 4705 (2023).
40. X. Lu, H. Shen, Y. Wei, H. Ge, J. Wang, H. Peng, W. Liu, Ultrafast growth and locomotion of dandelion-like microswarms with tubular micromotors. *Small* **16**, 2003678 (2020).
41. F. Soto, M. A. Lopez-Ramirez, I. Jeerapan, B. De Esteban-Fernandez Avila, R. K. Mishra, X. Lu, I. Chai, C. Chen, D. Kupor, A. Nourhani, J. Wang, Rotibot: Use of rotifers as self-propelling biohybrid microcleaners. *Adv. Funct. Mater.* **29**, 1900658 (2019).
42. Y. Lu, W. Tan, S. Mu, G. Zhu, Vortex-enhanced microfluidic chip for efficient mixing and particle capturing combining acoustics with inertia. *Anal. Chem.* **96**, 3859–3869 (2024).
43. Z. Zhakypov, K. Mori, K. Hosoda, J. Paik, Designing minimal and scalable insect-inspired multi-locomotion millirobots. *Nature* **571**, 381–386 (2019).
44. C. Fan, Y. Luo, T. Xu, Y. Song, X. Zhang, On-demand mixing and dispersion in mini-pillar based microdroplets. *Nanoscale* **13**, 739–745 (2021).

45. C. Zhang, X. Guo, P. Brunet, M. Costalonga, L. Royon, Acoustic streaming near a sharp structure and its mixing performance characterization. *Microfluid. Nanofluid.* **23**, 104 (2019).
46. H. Chen, Z. Yu, S. Bai, H. Lu, D. Xu, C. Chen, D. Liu, Y. Zhu, Microfluidic models of physiological or pathological flow shear stress for cell biology, disease modeling and drug development. *TrAC Trends Anal. Chem.* **117**, 186–199 (2019).
47. C. Souilhol, J. Serbanovic-Canic, M. Fragiadaki, T. J. Chico, V. Ridger, H. Roddie, P. C. Evans, Endothelial responses to shear stress in atherosclerosis: A novel role for developmental genes. *Nat. Rev. Cardiol.* **17**, 52–63 (2020).
48. C. L. Yankaskas, K. Bera, K. Stoletov, S. A. Serra, J. Carrillo-Garcia, S. Tuntithavornwat, P. Mistriotis, J. D. Lewis, M. A. Valverde, K. Konstantopoulos, The fluid shear stress sensor TRPM7 regulates tumor cell intravasation. *Sci. Adv.* **7**, eabh3457 (2021).
49. X. P. Zhang, C. Leung, Z. Lu, N. Esfandiari, R. F. Casper, Y. Sun, Controlled aspiration and positioning of biological cells in a micropipette. *IEEE Trans. Biomed. Eng.* **59**, 1032–1040 (2012).
50. M. Xie, A. Shakoor, Y. Shen, J. K. Mills, D. Sun, Out-of-plane rotation control of biological cells with a robot-tweezers manipulation system for orientation-based cell surgery. *IEEE Trans. Biomed. Eng.* **66**, 199–207 (2019).
51. J. Zhang, S. Yang, C. Chen, J. H. Hartman, P.-H. Huang, L. Wang, Z. Tian, P. Zhang, D. Faulkenberry, J. N. Meyer, T. J. Huang, Surface acoustic waves enable rotational manipulation of *Caenorhabditis elegans*. *Lab Chip* **19**, 984–992 (2019).
52. X. Liu, Y. Li, L. Li, M. Kojima, Q. Shi, Q. Huang, T. Fukuda, T. Arai, Noncontact 3-D orientation control at microscale: Hydrodynamic out-of-plane rotation and in-plane rotation by compacted rotational stage. *IEEE/ASME Trans. Mechatron.* **27**, 4807–4818 (2022).
53. J. Sun, B. Yang, N. Koukourakis, J. Guck, J. W. Czarske, AI-driven projection tomography with multicore fibre-optic cell rotation. *Nat. Commun.* **15**, 147 (2024).
54. A. Sorriento, M. B. Porfido, S. Mazzoleni, G. Calvosa, M. Tenucci, G. Ciuti, P. Dario, Optical and electromagnetic tracking systems for biomedical applications: A critical review on potentialities and limitations. *IEEE Rev. Biomed. Eng.* **13**, 212–232 (2019).
55. V. M. Gaspar, P. Lavrador, J. Borges, M. B. Oliveira, J. F. Mano, Advanced bottom-up engineering of living architectures. *Adv. Mater.* **32**, 1903975 (2020).
56. H. N. Oğuz, A. Prosperetti, The natural frequency of oscillation of gas bubbles in tubes. *J. Acoust. Soc. Am.* **103**, 3301–3308 (1998).
57. S. A. Elder, Cavitation microstreaming. *J. Acoust. Soc. Am.* **31**, 54–64 (1959).
58. D. L. Miller, Particle gathering and microstreaming near ultrasonically activated gas-filled micropores. *J. Acoust. Soc. Am.* **84**, 1378–1387 (1988).
59. M. F. Hamilton, D. T. Blackstock, *Nonlinear Acoustics* (Academic Press, 1998), vol. 237.
60. N. Nama, P.-H. Huang, T. J. Huang, F. Costanzo, Investigation of acoustic streaming patterns around oscillating sharp edges. *Lab Chip* **14**, 2824–2836 (2014).
61. N. Nama, R. Barnkob, Z. Mao, C. J. Kähler, F. Costanzo, T. J. Huang, Numerical study of acoustophoretic motion of particles in a PDMS microchannel driven by surface acoustic waves. *Lab Chip* **15**, 2700–2709 (2015).
62. W. L. Nyborg, Radiation pressure on a small rigid sphere. *J. Acoust. Soc. Am.* **42**, 947–952 (1967).
63. L. Feng, P. Di, F. Arai, High-precision motion of magnetic microrobot with ultrasonic levitation for 3-D rotation of single oocyte. *Int. J. Robot. Res.* **35**, 1445–1458 (2016).
64. E. Özelçi, E. Mailand, M. Rüegg, A. C. Oates, M. S. Sakar, Deconstructing body axis morphogenesis in zebrafish embryos using robot-assisted tissue micromanipulation. *Nat. Commun.* **13**, 7934 (2022).
65. S. V. Puttaswamy, N. Bhalla, C. Kelsey, G. Lubarsky, C. Lee, J. McLaughlin, Independent and grouped 3D cell rotation in a microfluidic device for bioimaging applications. *Biosens. Bioelectron.* **170**, 112661 (2020).
66. S. Zhang, E. Y. Scott, J. Singh, Y. Chen, Y. Zhang, M. Elsayed, M. D. Chamberlain, N. Shakiba, K. Adams, S. Yu, C. M. Morshead, P. W. Zandstra, A. R. Wheeler, The optoelectronic microrobot: A versatile toolbox for micromanipulation. *Proc. Natl. Acad. Sci. U.S.A.* **116**, 14823–14828 (2019).
67. R. Abedini-Nassab, S. Bahrami, Synchronous control of magnetic particles and magnetized cells in a tri-axial magnetic field. *Lab Chip* **21**, 1998–2007 (2021).
68. X. Tang, X. Liu, P. Li, D. Liu, M. Kojima, Q. Huang, T. Arai, Efficient single-cell mechanical measurement by integrating a cell arraying microfluidic device with magnetic tweezer. *IEEE Robot. Autom. Lett.* **6**, 2978–2984 (2021).
69. C. Leung, Z. Lu, X. P. Zhang, Y. Sun, Three-dimensional rotation of mouse embryos. *IEEE Trans. Biomed. Eng.* **59**, 1049–1056 (2012).
70. P. Pan, J. D. Laver, Z. Qin, Y. Zhou, R. Peng, L. Zhao, H. Xie, J. A. Calarco, X. Liu, On-chip rotation of *Caenorhabditis elegans* using microfluidic vortices. *Adv. Mat. Technol.* **6**, 2000575 (2021).
71. P. Vachon, S. Merugu, J. Sharma, A. Lal, E. J. Ng, Y. Koh, J. E.-Y. Lee, C. Lee, Cavity-agnostic acoustofluidic manipulations enabled by guided flexural waves on a membrane acoustic waveguide actuator. *Microsyst. Nanoeng.* **10**, 33 (2024).

Acknowledgments: We thank the staff of the Medical Center for Human Reproduction at Beijing Chaoyang Hospital, Capital Medical University (Beijing, China), for providing the experimental equipment and materials. **Funding:** This work was supported by the National Natural Science Foundation of China grant 62273052 (to X.L.), the Beijing Natural Science Foundation grant IS23062 (to T.A.), the Grants-in-Aid for Scientific Research from the Ministry of Education, Culture, Sports, Science and Technology of Japan 23K22712 (to T.A.), and the Jiangsu Natural Science Foundation grant BK20240856 (to Y.L.). **Author contributions:** Conceptualization: X.L., Y.L., T.A., and T.F. Methodology: X.L., Y.L., and T.A. Investigation: X.L., Y.L., F.L., Q.H., and T.A. Funding acquisition: X.L., Y.L., and T.A. Project administration: X.L., Y.L., Q.H., and T.A. Supervision: X.L., Y.L., Q.S., L.D., Q.H., T.A., and T.F. Writing—original draft: X.L. and Y.L. Writing—review and editing: X.L., Y.L., L.D., and T.A. Resources: X.L., Y.L., Q.S., and F.L. Validation: X.L., Y.L., and F.L. Formal analysis: X.L., Y.L., and F.L. Data curation: Y.L. Visualization: Y.L. **Competing interests:** The authors declare that they have no competing interests. **Data and materials availability:** All data needed to evaluate the conclusions in the paper are present in the paper and/or the Supplementary Materials.

Submitted 29 August 2024
Accepted 25 February 2025
Published 28 March 2025
10.1126/sciadv.ads8167